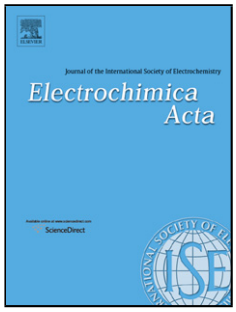

Title: On the effect of Sn-doping in hematite anodes for oxygen evolution

Author: Michele Orlandi Alberto Mazzi Giacomo Arban Nicola Bazzanella Paolo Rudatis Stefano Caramori Nainesh Patel Rohan Fernandes Carlo A. Bignozzi Antonio Miotello

PII: S0013-4686(16)31756-X
DOI: http://dx.doi.org/doi:10.1016/j.electacta.2016.08.046
Reference: EA 27824

To appear in: *Electrochimica Acta*

Received date: 25-5-2016
Revised date: 5-8-2016
Accepted date: 9-8-2016

Please cite this article as: Michele Orlandi, Alberto Mazzi, Giacomo Arban, Nicola Bazzanella, Paolo Rudatis, Stefano Caramori, Nainesh Patel, Rohan Fernandes, Carlo A.Bignozzi, Antonio Miotello, On the effect of Sn-doping in hematite anodes for oxygen evolution, Electrochimica Acta http://dx.doi.org/10.1016/j.electacta.2016.08.046

On the effect of Sn-doping in hematite anodes for oxygen evolution.

Michele Orlandi,[a]‡ Alberto Mazzi,[a]‡ Giacomo Arban,[a] Nicola Bazzanella,[a] Paolo Rudatis,[b] Stefano Caramori,[b] Nainesh Patel,[c] Rohan Fernandes,[c] Carlo A. Bignozzi,[b] Antonio Miotello.[a]*

[a] Dipartimento di Fisica, Università degli Studi di Trento, I-38123, Povo (Trento), Italy.

[b] Dipartimento di Scienze Chimiche e Farmaceutiche, Università degli Studi di Ferrara, Via Fossato di Mortara 17-19, 44100, Ferrara, Italy.

[c] Department of Physics, University of Mumbai, Vidyanagari, Santacruz (E), Mumbai 400 098, India.

Corresponding Author

* Dr. Michele Orlandi: michele.orlandi@unitn.it

Graphical abstract

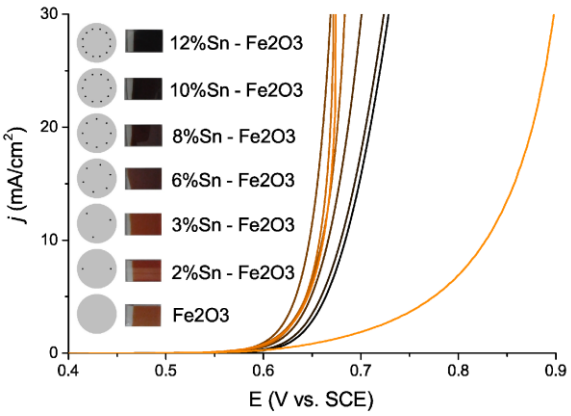

HIGHLIGHTS:

- a systematic investigation of the effects of tin doping in hematite anodes is given, with respect to structural, optical and electrochemical properties, focusing on the electrocatalysis of the oxygen evolution reaction;
- tin substitutional incorporation is obtained with a low-temperature procedure which leaves morphology and crystal phase unaltered, allowing to isolate the effect of tin doping on materials properties;
- optical absorption is progressively extended in the visible range due to a band-gap narrowing of about 0.45 eV for the highest doping level, likely due to sub-band gap states;
- greatly improved electrode metrics upon doping, with a shift of up to 60 mV towards less positive overpotentials and Tafel slopes about the half of the original value, are well explained by Tafel analysis and electrochemical impedance spectroscopy.

ABSTRACT Iron (III) oxide applications as anodic material in electrocatalysis and photoelectrochemical cells are currently limited by its poor electric properties. To overcome these issues, doping has been applied with some success and high-temperature (800°C) treatment on

fluorine doped tin oxide substrates, leading to tin-doping, is now a widely employed procedure to activate hematite anodes. In this paper we undertake a systematic investigation of the effects of tin doping on the structural, optical and electrochemical properties of hematite thin films, focusing on the anodic performance towards water splitting. To isolate the effect of doping from those of morphology and crystallinity, we devise a fabrication method based on radio-frequency magnetron sputtering yielding crystalline hematite at room temperature, thus enhancing the compatibility towards substrates and the potential for application. Doping in the range 1-12% (atomic) induces lattice distortion with cell volume increase and a substantial extension of the visible absorption range due to a band-gap narrowing of about 0.45 eV for the highest doping level. The electrode metrics are greatly improved, with a shift of up to 60 mV towards less positive overpotentials and Tafel slopes about the half of the original value. The best performance is found for a 6.2 at. % doping, with η=441 mV (at j=1 mA/cm^2) and a 48 mV/dec Tafel slope, in line with current state-of-the-art results reported for amorphous iron based catalysts. In our case tin doping leads to improved conductivity and to a decreased (up to 1 order of magnitude) interfacial charge transfer resistance, as revealed by electrochemical impedance spectroscopy.

KEYWORDS Fe_2O_3, tin-doping, magnetron sputtering, water splitting, electrocatalysis.

Abbreviations

RF-MS, radio-frequency magnetron sputtering, OER, oxygen evolution reaction, EIS, electrochemical impedance spectroscopy, CPE, constant phase element.

1. Introduction

In recent years iron oxides, conjugating earth-abundance and high market availability with their non-toxic and environmentally friendly nature, have attracted considerable attention for applications in catalysis where scalability[1],[2] is a central goal. Iron(III) oxide in particular, both amorphous (a-Fe_2O_3) and hematite (α-Fe_2O_3), has shown promising results as anodic material in electrochemical

and photoelectrochemical water splitting cells,[3-8] where it performs the oxygen evolution reaction (OER).

Hematite electrical properties are however far from ideal and severely limit its application as anodic material: in bulk form it is a Mott insulator, with resistivities of up to 10^{12} Ωcm and poor carrier mobility, especially for the hole minority carriers, for which it has a diffusion length of about 2-4 nm and a recombination lifetime in the ps range.[9] Among the strategies adopted to tackle these issues, nanostructuring features prominently.[10-12] In the past, doping by a variety of metals (Ti, Zr, Hf, V, Nb, W, Tl, Pb, Ge, Ce, Pt) has also been explored with mixed results.[13] The notable exception has been doping with a noble metal (Pt) which, along with surface modification with a cobalt phosphate co-catalyst, registered the highest photocurrents at now for a hematite based photoanode.[14] Recently, high temperature (800°C) thermal treatment of hematite photoanodes on fluorine doped tin oxide (FTO) substrates has been observed to greatly improve photocurrents and the effect has been attributed, among other factors, to tin doping by diffusion from the substrate.[3, 4] Tin is in itself a cheap, earth-abundant and non-hazardous metal, which would be an ideal dopant from the point of view of the materials scalability. Although the tin doping procedure by annealing has become a widely employed method to activate hematite photoanodes,[3, 15, 16] the current high temperature approaches are not ideal to investigate the nature and role of tin doping since the conditions required for incorporating tin into the crystalline hematite affect simultaneously various properties, such as the surface morphology and crystallinity of the hematite film as well as the conductivity of the FTO substrate, which play a critical role in determining the overall electrode performance in photoelectrochemical and electrochemical reactions. Additionally, the FTO resistivity has been reported to significantly increase above 600-700°C and most glass supports will undergo softening and warping with loss of their mechanical properties.[17, 18] The high temperature treatment is also not convenient in view of the scale-up to an industrial fabrication process, since it is energy-intensive and can damage both the electrode supports and substrates.

In this paper we undertake a systematic study of the effects of tin doping on hematite thin-films, with respect to structural, optical and electrochemical properties, investigating the catalytic

performance towards the OER in a water splitting cell. The method chosen for the hematite synthesis is Radio-Frequency Magnetron Sputtering (RF-MS), a physical vapor deposition technique which allows to carefully control the amount of dopant introduced. Using RF-MS we developed a fabrication process to obtain hematite films with a Sn content in the range 1-12 atomic %, as estimated by energy dispersive X-ray spectroscopy (EDS), which are already crystalline at room temperature, thus eliminating the need for a post-deposition thermal treatment. As a consequence, we could study the effect of increasing tin content without changing morphology and crystalline phase, thus decoupling the influence of surface modification and recrystallization which normally take place at high temperature. While surface morphology remains substantially unaltered, as revealed by scanning electron microscopy, a hematite lattice distortion resulting in an increasing cell volume, roughly linear with the tin content, is revealed by X-ray diffraction, micro Raman and XPS spectroscopy. Optical properties are deeply affected as well, with absorption spectra systematically extended in the UV-Vis range, following a decrease of the optical band-gap of up to 0.45 eV for the highest tin content. The electrode metrics with respect to water oxidation are also influenced by tin doping, leading to less positive overpotentials, shifted by as much as 60 mV, and halved Tafel slopes, yielding values that are comparable with those of state-of-the-art amorphous metal oxides and mixed-metal oxides or cobalt phosphates (Co-Pi).[5, 19] In this case the effect of tin doping is substantially an improvement of the film conductivity, which reflects in a decreased charge transfer resistance, as revealed by electrochemical impedance spectroscopy (EIS).

2. Experimental Section

2.1 Synthesis. Pure and Sn-doped αFe2O3 thin films were synthesized through RF-magnetron sputtering. The vacuum chamber was evacuated to a pressure lower than $4x10^{-7}$ mbar before deposition and a working pressure of $8x10^{-3}$ mbar was then obtained through an argon (99.99% purity) flux. An iron oxide disk was used as target (Sematrade, 99.5% purity Fe_2O_3, 10 cm diameter). The argon plasma was maintained through a RF power source working at 90W, 13.56

MHz. Substrates to target distance was fixed at 6.0 cm and the substrate holder was kept swinging in front of the target in order to improve film homogeneity. Crystalline hematite deposition was achieved without applying external substrate heating and without post-deposition treatments. The substrate temperature was monitored using a thermocouple in contact with the metallic substrate holder: during deposition, substrate temperature was weakly increasing and it reached approximately 60 °C after 90 minutes deposition. In order to remove surface contaminations from the target, a 20 minutes pre-sputtering treatment was performed before deposition at slightly higher argon pressure ($1x10^{-2}$ mbar). This simple and quick way to synthesize crystalline hematite was chosen after systematic variation of the sputtering parameters (RF power, pre-sputtering, argon pressure, substrate temperature). The same deposition parameters and procedure were employed to obtain tin-doped hematite: in that case a variable number of metallic Sn spheres were placed on the iron oxide target, close to the circular erosion profile.

Compact crystalline hematite films were deposited on 99.99% pure p-Si (100) slides and on fluorine doped tin oxide (FTO) coated glass electrodes. FTO-coated glass samples were cut as 15×25 mm slides and during sputtering deposition a small portion of the FTO area was hidden by an aluminum foil in order to preserve a free FTO contact. In order to perform structural and crystallographic characterization thick films were grown on Si (about 1 μm with 155 minutes deposition), while 200 nm thick hematite films were deposited on FTO electrodes through 31 minutes sputtering.

2.2 Materials characterization. Pure and tin-doped hematite films deposited on Si slides were analyzed through scanning electron microscopy (SEM-FEG, JSM 7001F, JEOL) at 20 keV electron beam energy. In order to evaluate dopant amount, energy dispersive X-ray spectroscopy was employed (EDS, INCA PentaFET-x3). The vibrational modes and short-range order of films deposited on FTO substrates were studied via Raman spectroscopy, using a Labram Aramis Jobin-Yvon Horiba μ-Raman apparatus equipped with a He-Ne laser source (632.8 nm). Furthermore we studied prevalent crystallites orientation and long range order of thick films deposited on Si substrates through X-ray diffraction (XRD) in Bragg-Brentano θ-2θ configuration, exploring the

10°÷100° 2θ range with a step size of 0.05° and a scan rate of 0.01°/s. As X-ray source for XRD analysis we employed the monochromatic Cu K_α emission (λ=1.5414 Å). X-ray photoelectron spectroscopy (XPS) was acquired using a PHI 5000 VersaProbe II equipped with a mono-chromatic Al K_α (1486.6 eV) X-ray source and a hemispherical analyzer. Electrical charge compensation was required to perform the XPS analysis. The sample was analyzed at the surface (without pre-sputtering), after sputtering for 2 minutes with a 1 kV Ar beam and after sputtering for 8 minutes to reach the bulk of the samples. All the binding energies were referenced to the C1s peak at 284.8 eV and reference binding energies (BE) are reported as the average value of all references included in the NIST X-ray Photoelectron Spectroscopy Database.[20]

The effect of doping on optical properties of hematite was investigated through a UV-VIS-NIR absorption spectrophotometer (Varian Cary 5000 UV-VIS-NIR absorption spectrometer).

2.3 Electrochemical measurements. Electrochemical and photoelectrochemical measurements were performed with an Eco Chemie Autolab PGSTAT 302/N apparatus in a three-electrode cell composed of a saturated calomel electrode (SCE, 0.244 V *versus* standard hydrogen electrode SHE) as reference, platinum counter electrode and a 1 M KOH electrolyte solution (pH 14). Glass/FTO/hematite samples were used as working electrodes (1 cm^2 active area). Copper tape was applied to the bare portion of FTO in order to optimize electrical connection with the electrode holder. Linear sweep voltammetry (LSV) measurements were collected with scan rate of 10 mV/s in static solution, with applied *iR* compensation. For photoelectrochemical measurements the illumination source was an ABET solar simulator (AM 1.5G, 100 mW/cm^2).

Electrochemical impedance spectroscopy (EIS): EIS experiments were carried out in aqueous 2 M KOH in the dark, by applying a sinusoidal 10 mV perturbation in the frequency range between 10^5 and 10^{-2} Hz. In order to address the kinetics of the faradic processes, experiments were carried out by sampling the rising part (0.6-1V vs SCE) of the *j/V* curves at 50 mV intervals. In order to investigate the physical nature of the high-frequency capacitive response of the electrodes (CPE1, Scheme 1), a high frequency (10^5-10^2 Hz) scan was performed in the potential interval between 0 and 0.5 V vs SCE, before the onset of the anodic discharge. A good fit of the impedance data was

achieved with the model reported in Scheme 1 where R1 accounts for the ohmic contribution of the electrochemical cell (contact and solution resistance) the R3/CPE2 mesh models the electrolyte/hematite interface and R2/CPE1 describes the depletion layer which should develop in the relatively compact micrometric hematite layers under study. CPE is the constant phase element modeling the non ideal electrochemical capacitance. In our case the CPE exponent was always comprised between 0.85 and 0.98.

3. Results and discussion

3.1 Film deposition and morphology. Pure and tin-doped hematite was deposited on Si and FTO-coated glass slides. Tin doping in the percentage range 1÷12% (expressed as Sn/(Sn+Fe) atomic ratio) was obtained by placing on the Fe_2O_3 target a variable number of metallic Sn small spheres (of about 50 mg weight and of the same size) as shown in Figure 1.

While Sn spheres were usually placed on the plasma erosion profile, 1.2 at. % Sn-doped samples were obtained by placing two Sn spheres about 5 mm outside the plasma track. The picture of a set of samples with increasing dopant loading (Figure 1) clearly shows the color change due to tin doping. Tin percentage was evaluated by EDS measurements and the results are summarized in Table 1.

α-Fe_2O_3 and Sn-doped α-Fe_2O_3 films about 1.2 μm thick were deposited on Si slides. The deposited film showed a compact structure with jagged surface morphology (Figure 2). The nearly constant film morphology, together with its compactness, allows us to study the role of dopant loading on electrochemical and optical properties decoupled from morphology effects. It is worth to note that usual experimental procedures to synthesize Sn-doped hematite such as chemical preparation routes and the annealing of pure hematite films on tin-containing substrates generally cause significant morphological modifications.[3, 4, 21, 22]

3.2 Raman spectroscopy. Thin films with variable Sn loading deposited on glass-FTO substrates showed the presence of hematite Raman response (figure 3). The spectra showed the vibrational modes of hematite, in particular two A_{1g} modes (219.6 and 492.3 cm^{-1}) and five E_g modes (236.5, 282.7, 295.2, 395.9 and 596.0 cm^{-1}). A peak was also detected at 660 cm^{-1} and it can be explained as the activation of the E_u longitudinal optical mode, that is IR active and appears due to the disorder in the hematite lattice.[23]

The different intensities and the broadening of the Raman active modes can be explained through a combination of several factors: stress induced by the presence of Sn, size of the crystallites, film thickness. In our case the crystallite size, as estimated from XRD peaks broadening by using the Scherrer relation, does not vary significantly and no systematic behavior due to the progressive presence of Sn can be recognized (see Table S1 for both the relation and the data). It is worth noting that the crystallites visible in the top-down SEM image for the 12 at. % samples (Figure 2) are apparently of larger size than estimated in Table S1. This is likely due to a slightly different columnar growth, with less void space between the crystallites and less well-defined boundaries. The apparently larger surface features arise then from closely-packed but still largely distinct columnar structures, which have a lateral size in agreement with the XRD estimated values and similar to that of the undoped sample. This can be appreciated from the SEM images reported in Figure S1, showing an higher magnification detail of the cross-section for both the 0% and the 12% samples.

Since the film thickness is kept constant, we consider lattice distortion caused by doping as the main reason for the Raman peaks broadening.

3.3 X-ray diffraction. XRD analysis proved the presence of hematite hexagonal structure as the sole detectable crystalline phase in the deposited films. Rietveld refinement was performed with the Maud software,[24] using a March–Dollase texture profile about the (300) hematite plane to account for preferential orientation. The (300) plane, detected at 64.02° in the pure hematite sample, appeared to be the preferred one, allowing good signal fitting for all the dopant loadings. On the other hand, on the base of our analysis, the (110) reflection resulted to be always in minority,

though present in all the spectra (figure 4). Since hematite shows a highly anisotropic conductivity and (110) orientation has been proved to be the most favorable one in hematite photoanodes,[25] this could explain the absence of a significant photocatalytic activity of our electrodes deposited on FTO.

The phase composition of the films was studied by using as reference the crystalline structures of hematite (Fe2O3) and cassiterite (SnO2) taken from Maud structure database [24] and from the Crystallography Open Database,[26] respectively. The Rietveld analysis performed on the diffraction spectrum of the 12.4 at. % sample including the two phases showed that the eventual amount of tin oxide as a distinct phase is below the technique resolution (figure S2).

Peak positions and relative intensities undergo slight modifications with increasing dopant amount. The cell parameters a and c were extracted from the Rietveld analysis discussed above. The fitting parameters are reported in Table 2, while a typical plot of the fit function is reported in Supporting Information (figure S2). As displayed in Figure 5, the hematite hexagonal structure is strained by tin loading, with a progressive elongation of *a* and *b* parameters, and contraction of *c*. The result of the lattice distortion is an approximately linear growth of cell volume as a function of the dopant concentration, as clearly shown in Figure 5. In conclusion, XRD characterization proves that in our samples tin atoms are substitutionally located in the hematite lattice.

3.4 XPS analysis. XPS spectra were taken both at the surface and in the bulk of the films to investigate the oxidation state of tin and iron. While it is not possible to distinguish between Sn^{2+} and Sn^{4+} due to the strong overlap of their signals[27, 28] (Sn3d5/2 BE = 486.5 ± 0.6 eV and BE = 486.6 ± 0.3 eV respectively), the presence of Sn(0) (BE = 485.0 ± 0.5 eV)[20] can be considered negligible even for the highest tin content films. The spectrum for the 12 at. % sample is reported as an example in figure S1. Only Fe(III) is detected but, in comparison to pure hematite, the BE for Fe2p signals (Fe2p3/2 peak BE = 710.2 ± 0.5 eV and Fe2p1/2 peak BE = 723.7 ± 0.5 eV)[20] are positively shifted by 0.65-0.85 eV for all the Sn doped samples (Fig S3). These results indicate that

Sn is substitutionally incorporated in the hematite lattice, thus altering the chemical environment of Fe and are in good agreement with XRD and micro Raman.

3.5 Optical properties. UV-Vis-NIR absorption spectroscopy allowed us to study the effect of tin doping on hematite optical properties (Fig. 6). The samples with high Sn at. % (≳6 at. %) show an improved absorption in the entire investigated range and present a progressive absorption range extension toward the infrared region. In order to quantify the absorption range extension Tauc analysis was performed for both direct and indirect transitions, both of which are reported in literature for hematite.[29] The absorption coefficient was calculated as $\alpha = {}^{A}/_{d \log_{10} e}$, where A is the absorbance and d the film thickness. Tauc plots in Figure S4 display the quantity $(\alpha h\nu)^{1/r}$ as a function of photon energy, where $r = 1/2$ for direct transitions and $r = 2$ for indirect transitions. The linear fits that allow us to estimate the optical band gap were carried out in the range [2.27÷2.42] eV and [2.40÷2.60] eV for direct and indirect transitions, respectively. In case of high Sn loading (8, 10, 12 at. %) a direct transition was not clearly observed. In Table 3 we show the calculated band gaps and especially in the case of indirect transition it is possible to observe a clear band gap reduction of about 0.45 eV at high tin at. %. In conclusion we experimentally proved that intermediate doping (≈6 at. % Sn) causes band gap reduction due to formation of sub-band gap states originated by the introduction of dopant atoms, while at higher Sn percentage the band structure is more deeply altered by the disappearance of the direct transition. These results are in agreement with recent computational work on tin-doped hematite.[30]

3.6 Electrochemistry. The hematite and tin-doped hematite films deposited on FTO electrodes were tested for electrochemical and photoelectrochemical water oxidation in a three-electrode configuration cell. Before measurement, the electrodes were subjected to voltammetry cycles in the potential range -0.24÷1.76 V *versus* SCE in order to obtain a stable response and to remove eventual surface impurities. The *j/V* characteristics under dark conditions with *iR* compensation are shown in Figure 7, with the inset showing Tafel plots. The electrode metrics obtained by Tafel analysis (overpotential at j=1 mA/cm^2 and Tafel slopes) are summarized in Table 4. It is

immediately evident that all Sn:Fe_2O_3 are better OER catalysts than their undoped counterpart, with the best performance for Sn concentration in the range 2÷6 at. % Sn. In particular the best results were found for the 6.2 at. % sample, which exhibits 441 mV overpotential at 1 mA/cm^2 and 48 mV/dec Tafel slope (see Table 4 for details).

It is worth noting that the high Tafel slope of the pure hematite film is halved by introducing Sn: this result has to be attributed to doping since the films have negligible difference in terms of surface morphology, crystallite orientation and film thickness. The electrocatalytic activity of the tin-doped hematite compact films deposited by RF-magnetron sputtering are comparable with that of nanostructured amorphous Fe_2O_3 thin coatings synthesized by pulsed laser deposition[6] (η= 497 mV at 0.2 mA/cm^2, b = 35.6 mV/dec) or photochemical metal-organic deposition[5] (η= 400 mV at 0.5 mA/cm^2, b = 40 mV/dec). This is remarkable for compact bulk-like films as the ones under study and indicates great potential for improvement by introducing nanostructuring.

The reason for the enhanced OER catalysis performance lies essentially in a significant reduction of both the R2 resistance and the charge transfer resistance (R3), consistent with both improved conductivity and better electrocatalytic ability of the tin doped hematite films (Figure 8) where each resistive element (R1, R2 and R3) is plotted as a function of the applied potential. In both unmodified hematite (Figure 8 A) and in the 6.17 at. % (Figure 8 B) Sn doped sample the ohmic resistance accounting for the cell resistance is essentially the same, ca. 20 Ohm, expectedly independent from the potential, and in agreement with the typical ohmic resistance of the FTO back contact. In both substrates R3 decreases exponentially with the applied potential, in agreement with the high field approximation of the Butler-Volmer equation, and was thus assigned to the charge transfer resistance (R_{CT}), being about one order of magnitude larger in unmodified hematite with respect to the best performing Sn doped sample.

In the 0 at. % doped Fe_2O_3 electrode R2 represents the major resistive contribution and decreases exponentially with the applied potential, while in the 6.17 % Sn doped sample this contribution is the smallest and is substantially independent from the potential. The summed individual resistive contributions describe both qualitatively and quantitatively well the *j/V* response of the electrode,

as can be appreciated from Figure 8 C-D, where the derivative of the current-voltage curve is compared to R_{TOT}^{-1} where $R_{tot}=R_1+R_2+R_3$. It can be clearly observed from Figures 8 B and D that in the doped sample it is the ohmic R1 (principally the resistance of the ohmic collector) the dominating factor in controlling the *j/V* response of the cell, whereas R2 and R3 are on average less than 10 times smaller than the former. By contrast, in the unmodified sample, the electrochemical response is largely limited by both the R2 component and by the charge transfer resistance (R3), with the three resistive contributions becoming relatively comparable in magnitude only at strong positive potential, i.e. for V > 0.9 V vs SCE.

The study of the high frequency capacitive response allows to shine some light on the physical nature of the R2/CPE1 element which has a seemingly different nature in the two different electrodes. In the unmodified hematite film, the CPE1 capacitance followed well the Mott Schottky (MS) behavior (Figure S5). Although a little frequency dispersion is observed, probably due to the porous nature of the micrometric film, the linear MS plots taken at different frequencies agree in individuating the flat band potential at -2.00 ± 0.03 V vs SCE, a value consistent with the optical band gap (ca. 2.1 eV) and with the valence band edge (ca. 0.1 V vs SCE) estimated electrochemically from the onset of the anodic process at ca. 0.6 V vs SCE, taking into consideration the overpotential (ca. 0.5 V) for the water oxidation process. This implies that hole injection into the electrolyte is controlled by the formation of the depletion layer within the compact film which assists hole migration at the interface with the electrolyte where charge transfer occurs. Accordingly, since this process involves the transfer across the bulk electrode, its associated resistance, R2, is high, given the poor conductivity of unmodified hematite. By contrast, the Sn doped samples does not exhibit any convincing MS behavior at comparable frequencies, the high frequency capacitance showing instead a broad distribution with nearly constant values (Figure S6) before electrode depolarization by anodic discharge occurs at ca. 0.5 V vs SCE, a behavior consistent with the emptying of intra-band gap states on which the Fermi level may be pinned, as in degenerate semiconductors. The presence of intraband donor states from which electrons are easily removed is consistent with the reduced resistance observed for such process, explaining the

improved conductivity of the doped films. A further contribution to the improved conductivity may arise from a reduction of the effective electron mass, as these are inversely proportional quantities for an n-type semiconductor. As recently predicted by theoretical modeling based on first-principles calculations,[30] tin doping in the range 1-16 at. % is indeed expected to induce a decrease in the effective electron mass irrespective of the Miller plane considered.

Despite the enhanced light absorption properties discussed above, all these electrodes did not show a satisfactory photocurrent response if compared to nanostructured films with optimized morphology. This has to be attributed to a combination of film thickness, compact morphology and unfavorable crystallite orientation. In fact it is known in literature that non-porous hematite films with thickness of some micrometers can show significant photocurrents[31] and that crystallite prevalent orientation can determine the photocatalytic activity[25] by overcoming the issue of the small carrier diffusion length of hematite with a preferential charge transport toward the desired direction. Nevertheless, photoelectrochemical results (Figure S7) show an enhanced response of the tin doped substrates in the 6-12 at. % range, consistent with the improved electrochemical properties observed in dark electrochemical experiments.

In addition, constant potential electrolysis carried out on the 7.7. % Sn-doped sample at 1 V *versus* SCE in 1M KOH (Figure 9), without iR drop compensation, showed a current variation smaller than 3 % during a 120 minute test, testifying an appreciable film stability.

4. Conclusion

In this work we developed a synthetic procedure for tin-doped hematite based on RF-MS and proceeded to fabricate thin-films with a controlled content of Sn in the range 1-12 at. % (Sn/Sn+Fe). This procedure is in itself an advancement over current fabrication techniques since crystalline tin-doped hematite could be obtained at room temperature, without relying on energy-intensive and potentially substrate-damaging post-fabrication thermal treatments. Moreover, this allowed us to systematically vary the Sn content without significantly altering the surface morphology and the crystal phase of the samples, which are determinant for the OER catalysis

performance, thus effectively surveying the effects of an increasing tin content on the structural, optical and electrochemical properties of the material.

Doping in the range 1-12 at. % leads to hematite lattice distortion consistent with the presence of tin atoms as substitutional dopants which is substantially linear with the Sn/Fe ratio. The optical absorption in the visible range is greatly extended due to band-gap narrowing, though this is not paralleled by the appearance of a significant photoelectrochemical activity. The reason for this behavior is likely a combination of unfavorable crystalline planes orientation, compact morphology limiting solvent permeation and excessive thickness compared to the typical carrier diffusion length of hematite.

The electrode metrics with respect to the electrochemical OER are improved by doping, resulting in much better charge transport and transfer properties with respect to the unmodified counterpart. The Tafel analysis revealed the best performance in the case of 6.2 % sample, which exhibits 441 mV overpotential at j=1 mA/cm^2 and 48 mV/dec Tafel slope. Although overpotentials are in the usual range for hematite anodes, Tafel slopes of the tin doped samples are in line with state-of the-art catalysts, e.g amorphous mixed-metal-oxides and CoPi, and point out their promising application in electrocatalytic water oxidation.

While useful for a first systematic investigation of tin-doping effects, the synthetic procedure developed in this paper does not allow to pursue the nanostructuring strategy, which should further improve their performance in OER and is likely essential to enable the efficient extraction of photo-generated electrons, thus allowing to extend our investigation to photoelectrochemical applications. Future work will then focus on the possibility of inducing nanostructures with RF-MS by tuning deposition pressure and temperature according to Thornton's Structure-Zone diagram.[32]

Author Contributions

The manuscript was written through contributions of all authors. All authors have given approval to the final version of the manuscript. ‡ These authors contributed equally to the manuscript.

Funding Sources

The research activity is partially supported by the PAT (Provincia Autonoma di Trento) project ENAM in cooperation with Istituto PCB of CNR (Italy). FIRB Project Nanosolar is gratefully acknowledged for funding (UNIFE).

Acknowledgements

We gratefully acknowledge Claudio Cestari for technical help and Dr. Cristina Armellini for X-ray diffraction measurements. The authors are indebted to Dr. Mauro Bortolotti for useful discussions and for precious support in the use of Maud software. R. Fernandes and N. Patel acknowledge UGC for providing financial support through Dr. D. S. Kothari postdoctoral fellowship program and Faculty recharge program respectively.

REFERENCES

[1] P.C.K. Vesborg, T.F. Jaramillo, RSC Advances, 2 (2012) 7933.
[2] M.D. Bhatt, J.S. Lee, J. Mater. Chem. A, 3 (2015) 10632-10659.
[3] K. Sivula, R. Zboril, F. Le Formal, R. Robert, A. Weidenkaff, J. Tucek, J. Frydrych, M. Grätzel, Journal of the American Chemical Society, 132 (2010) 7436-7444.
[4] Y. Ling, G. Wang, D.A. Wheeler, J.Z. Zhang, Y. Li, Nano letters, 11 (2011) 2119-2125.
[5] R.D. Smith, M.S. Prevot, R.D. Fagan, Z. Zhang, P.A. Sedach, M.K. Siu, S. Trudel, C.P. Berlinguette, Science, 340 (2013) 60-63.
[6] M. Orlandi, S. Caramori, F. Ronconi, C.A. Bignozzi, Z. El Koura, N. Bazzanella, L. Meda, A. Miotello, ACS applied materials & interfaces, 6 (2014) 6186-6190.
[7] L. Trotochaud, J.K. Ranney, K.N. Williams, S.W. Boettcher, Journal of the American Chemical Society, 134 (2012) 17253-17261.
[8] N. Dalle Carbonare, S. Carli, R. Argazzi, M. Orlandi, N. Bazzanella, A. Miotello, S. Caramori, C.A. Bignozzi, Physical Chemistry Chemical Physics, 17 (2015) 29661-29670.
[9] F.E. Osterloh, Chemical Society reviews, 42 (2013) 2294-2320.
[10] A. Kay, I. Cesar, M. Grätzel, Journal of the American Chemical Society, 128 (2006) 15714-15721.
[11] B.M. Klahr, A.B. Martinson, T.W. Hamann, Langmuir : the ACS journal of surfaces and colloids, 27 (2011) 461-468.
[12] V. Cristino, S. Berardi, S. Caramori, R. Argazzi, S. Carli, L. Meda, A. Tacca, C.A. Bignozzi, Physical chemistry chemical physics : PCCP, 15 (2013) 13083-13092.
[13] L. Vayssieres, On Solar Hydrogen & Nanotechnology, John Wiley & Sons (Asia), 2009.
[14] J.Y. Kim, G. Magesh, D.H. Youn, J.-W. Jang, J. Kubota, K. Domen, J.S. Lee, Scientific Reports, 3 (2013) 2681.
[15] C.D. Bohn, A.K. Agrawal, E.C. Walter, M.D. Vaudin, A.A. Herzing, P.M. Haney, A.A. Talin, V.A. Szalai, The Journal of Physical Chemistry C, 116 (2012) 15290-15296.

[16] J. Frydrych, L. Machala, J. Tucek, K. Siskova, J. Filip, J. Pechousek, K. Safarova, M. Vondracek, J.H. Seo, O. Schneeweiss, M. Gratzel, K. Sivula, R. Zboril, Journal of Materials Chemistry, 22 (2012) 23232-23239.
[17] H. Zhao, J. Kiwi, C. Pulgarin, J. Yang, International Journal of Applied Glass Science, 4 (2013) 242-247.
[18] J.K. Yang, B. Liang, M.J. Zhao, Y. Gao, F.C. Zhang, H.L. Zhao, Scientific Reports, 5 (2015) 15001.
[19] Y. Surendranath, M.W. Kanan, D.G. Nocera, Journal of the American Chemical Society, 132 (2010) 16501-16509.
[20] NIST X-ray Photoelectron Spectroscopy Database, in, http://srdata.nist.gov/xps/ National Institute of Standards and Technology, Gaithersburg, 2012.
[21] J. Cai, S. Li, Z. Li, J. Wang, Y. Ren, G. Qin, Journal of Alloys and Compounds, 574 (2013) 421-426.
[22] H.K. Dunn, J.M. Feckl, A. Muller, D. Fattakhova-Rohlfing, S.G. Morehead, J. Roos, L.M. Peter, C. Scheu, T. Bein, Physical Chemistry Chemical Physics, 16 (2014) 24610-24620.
[23] A.M. Jubb, H.C. Allen, ACS applied materials & interfaces, 2 (2010) 2804-2812.
[24] Maud: Materials Analysis Using Diffraction, Version 2.68, 2016, http://maud.radiographema.eu/.
[25] S. Kment, P. Schmuki, Z. Hubicka, L. Machala, R. Kirchgeorg, N. Liu, L. Wang, K. Lee, J. Olejnicek, M. Cada, I. Gregora, R. Zboril, ACS Nano, 9 (2015) 7113-7123.
[26] S. Gražulis, A. Daškevič, A. Merkys, D. Chateigner, L. Lutterotti, M. Quirós, N. R. Serebryanaya, P. Moeck, R.T. Downs, A. LeBail, Nucleic Acids Research 40 (2012) D420-D427.
[27] J.A. Rodriguez, T. Jirsak, S. Chaturvedi, J. Hrbek, Journal of the American Chemical Society, 120 (1998) 11149-11157.
[28] G.J. Siri, J.M. Ramallo-López, M.L. Casella, J.L.G. Fierro, F.G. Requejo, O.A. Ferretti, Applied Catalysis A: General, 278 (2005) 239-249.
[29] V.R.D. Satsangi, S.; Shrivastav, R. , Nanostructured A-Fe2o3 in Pec Generation of Hydrogen., in: L. Vassyeres (Ed.) On Solar Hydrogen & Nanotechnology, 2010, pp. 349-397.
[30] X. Meng, G. Qin, W.A. Goddard, S. Li, H. Pan, X. Wen, Y. Qin, L. Zuo, The Journal of Physical Chemistry C, 117 (2013) 3779-3784.
[31] K.G. Upul Wijayantha, S. Saremi-Yarahmadi, L.M. Peter, Physical Chemistry Chemical Physics, 13 (2011) 5264-5270.
[32] J.A. Thornton, Journal of Vacuum Science and Technology, 11 (1974) 666-670.

Figures

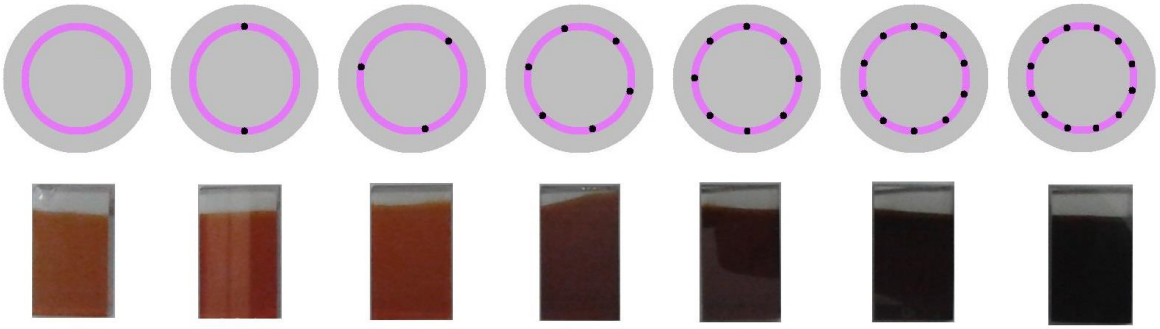

Figure 1. Target arrangement and picture of the FTO/hematite electrodes with variable Sn amount. The light purple circle represents the plasma track. The black dots correspond to Sn spheres positions. These target configurations resulted in 0, 1.9, 3.0, 6.2, 7.7, 9.5, 12.4 Sn nominal atomic percentage, respectively.

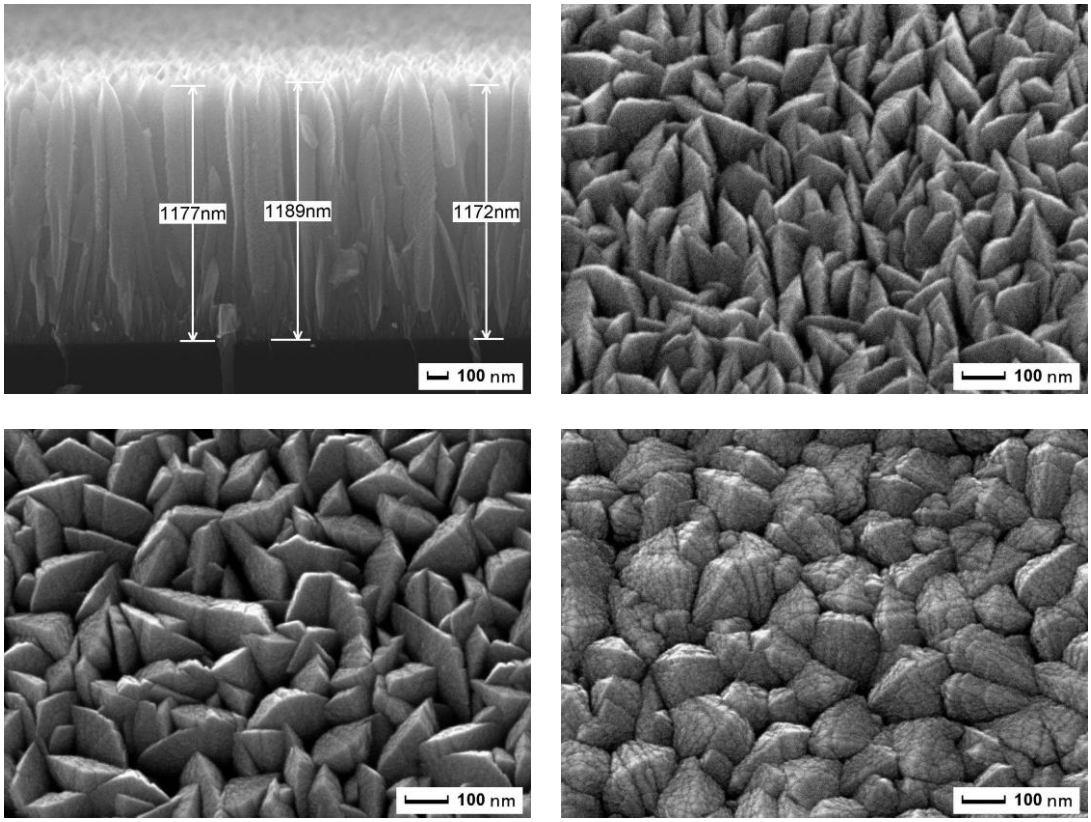

Figure 2. (top) Cross section and top view SEM images of pure αFe_2O_3 deposited on silicon; (bottom) Top view SEM images of 6 at. % and 12 at. % tin-doped αFe_2O_3.

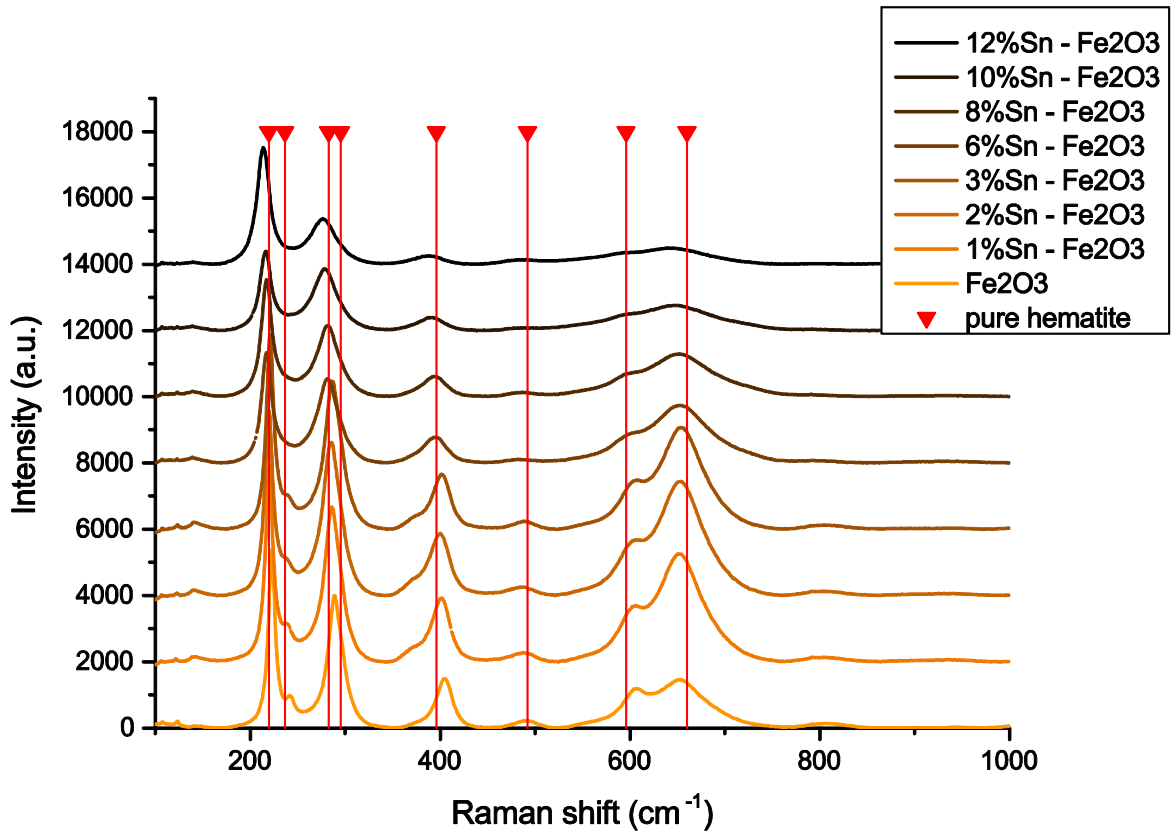

Figure 3. μ-Raman spectra of pure and tin-doped hematite films on glass/FTO substrates.

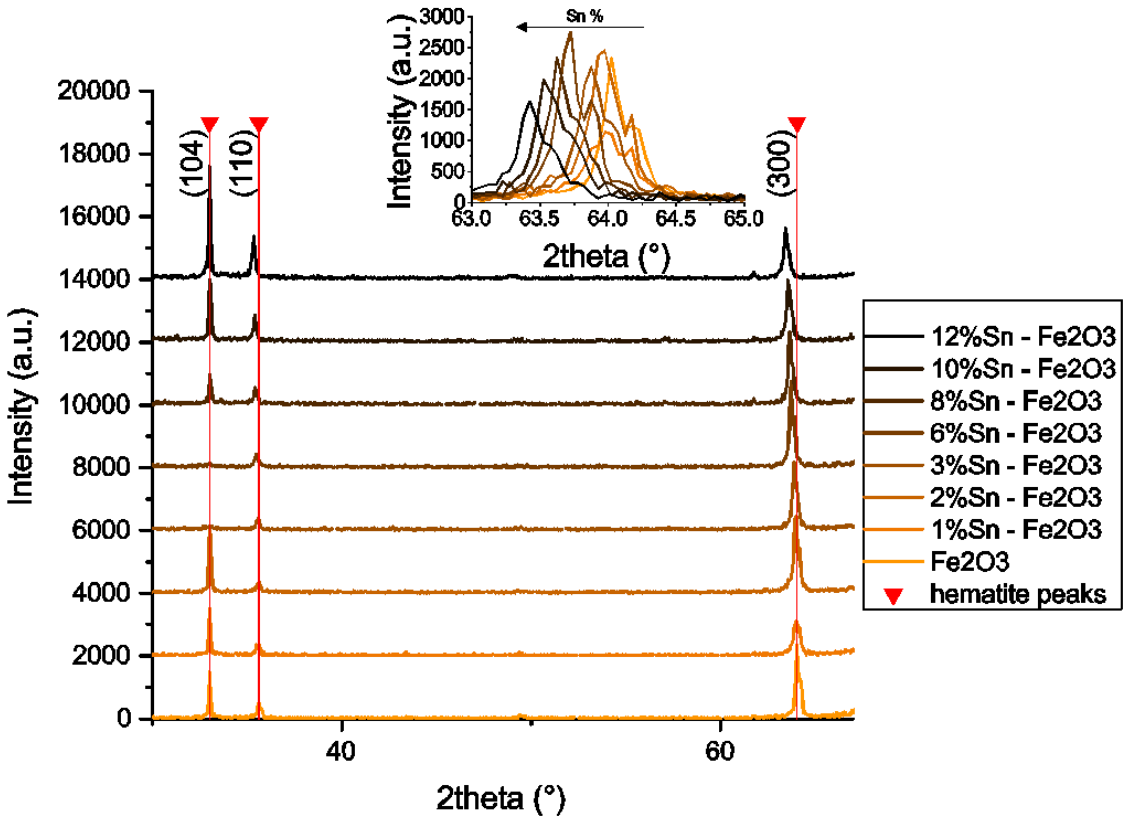

Figure 4. XRD spectra of pure and tin-doped hematite (the plot is limited to the range with significant signal). The most intense peaks correspond to (104), (110) and (300) planes. The inset shows (300) peak shifting with different Sn at. %.

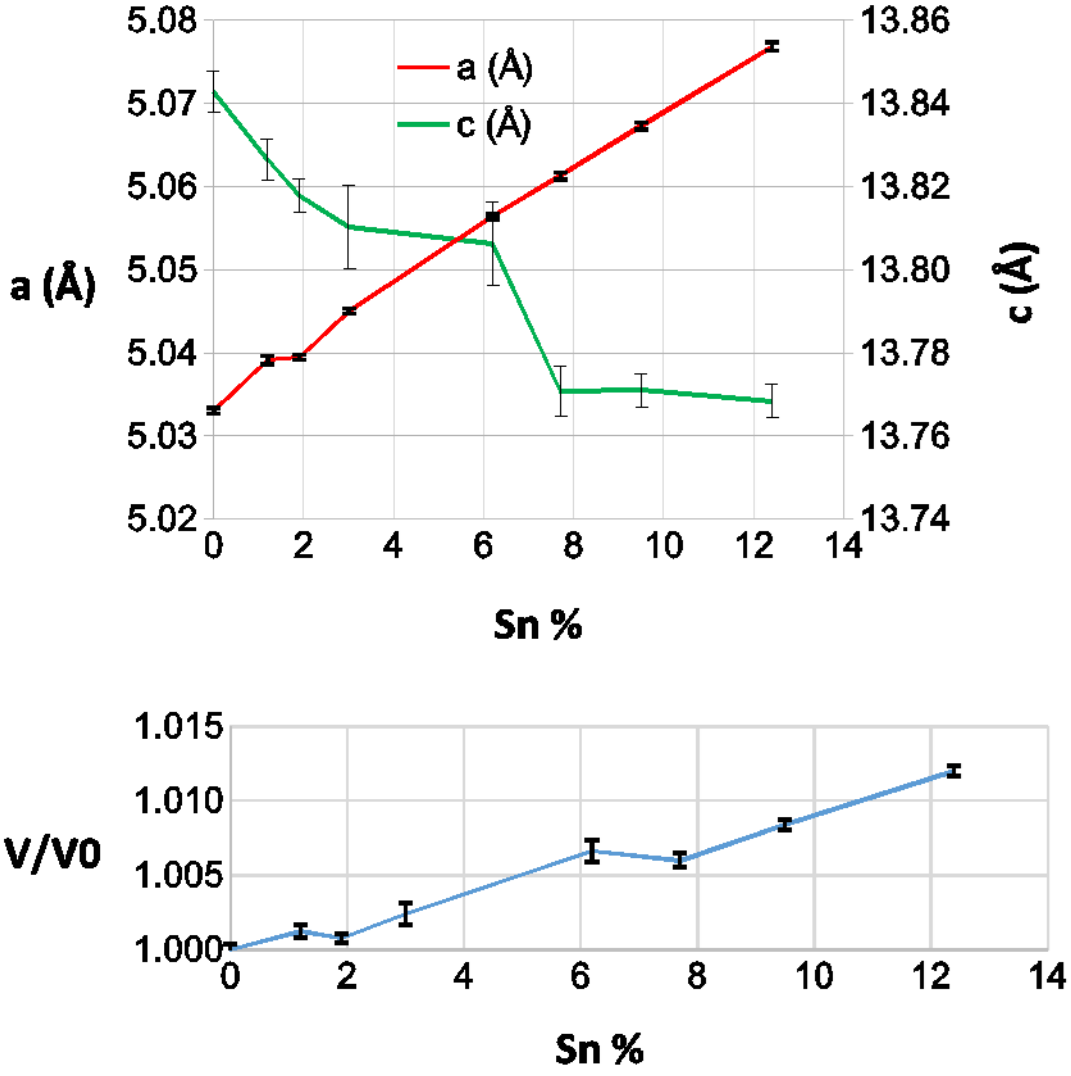

Figure 5. (top) Cell parameters *a* and *c* extracted from Rietveld refinement of XRD spectra. (bottom) Cell volume relatively to pure hematite.

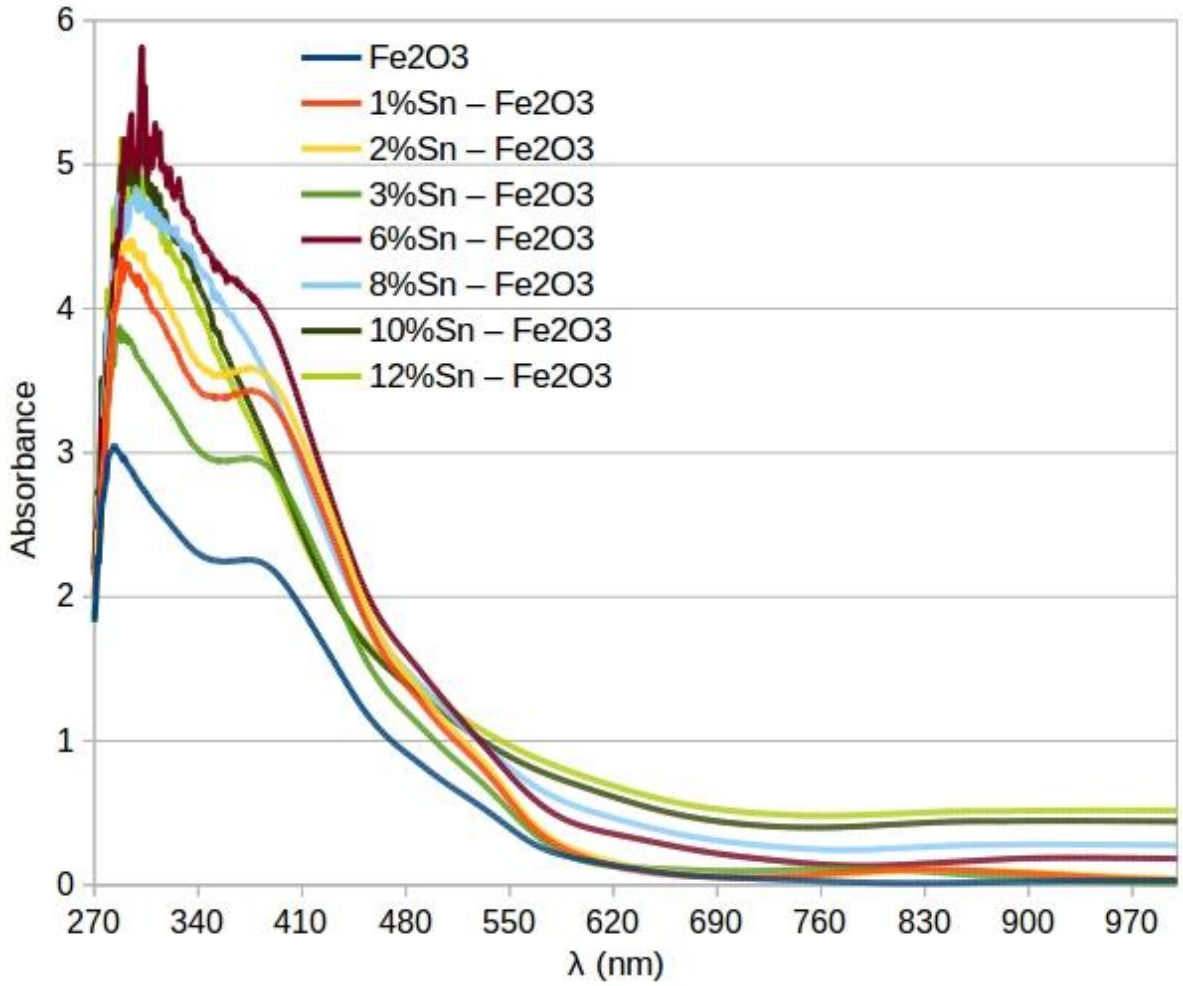

Figure 6. Absorbance spectra of pure and tin-doped hematite films on glass/FTO substrates.

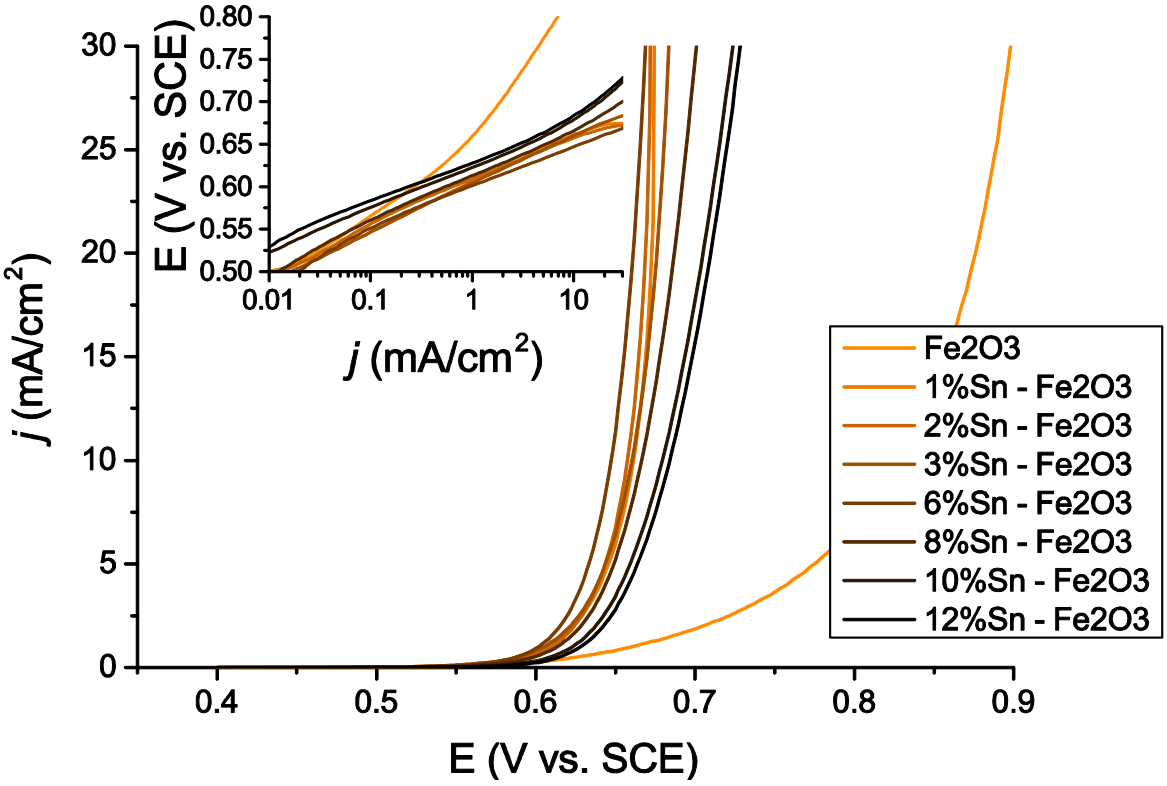

Figure 7. LSVs under dark conditions of pure and tin-doped hematite films deposited on FTO electrodes. *iR* compensation was applied. In the inset, the same data are displayed as a Tafel plot.

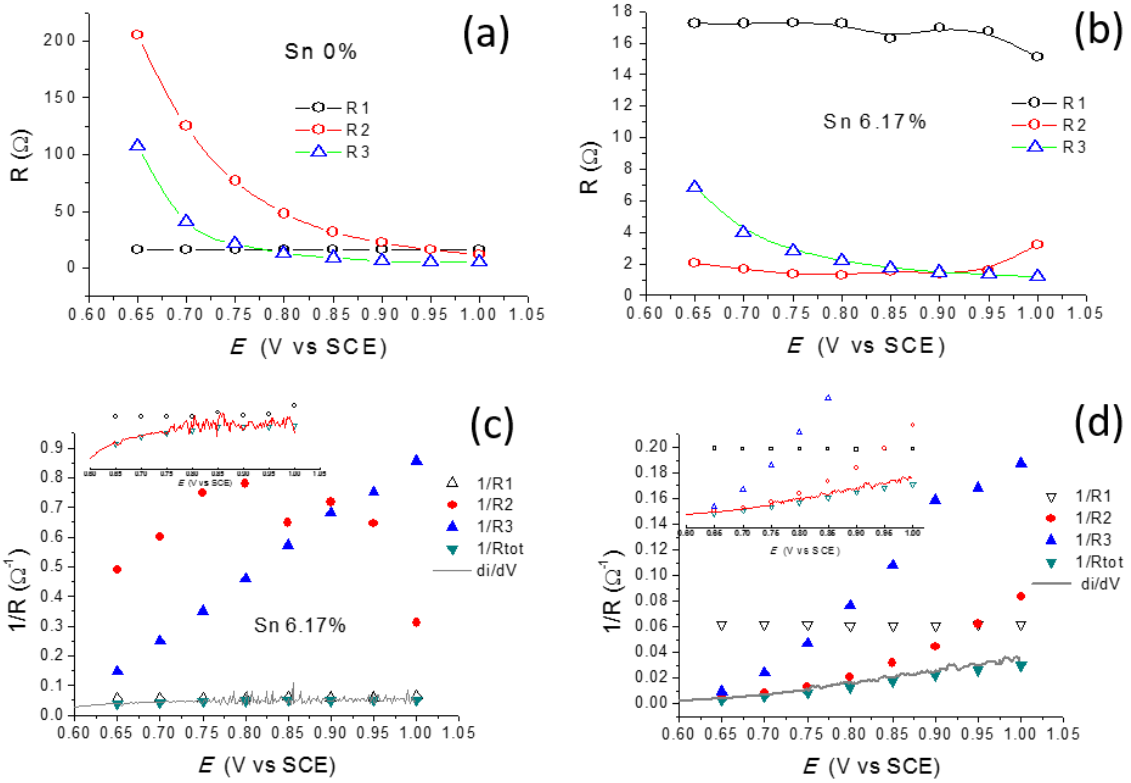

Figure 8. (A) and (B) individual resistive contributions *vs* applied voltage in unmodified hematite and 6.17 at. % Sn doped anodes; (C) and (D): Reciprocal of the individual resistances (R_i^{-1}) and their sum (R_{TOT}^{-1}, green upside-down triangle) compared to $\delta i/\delta V$ (grey line). 2 M KOH. Inset: magnification of the $\delta i/\delta V$ vs R_{TOT}^{-1} plot.

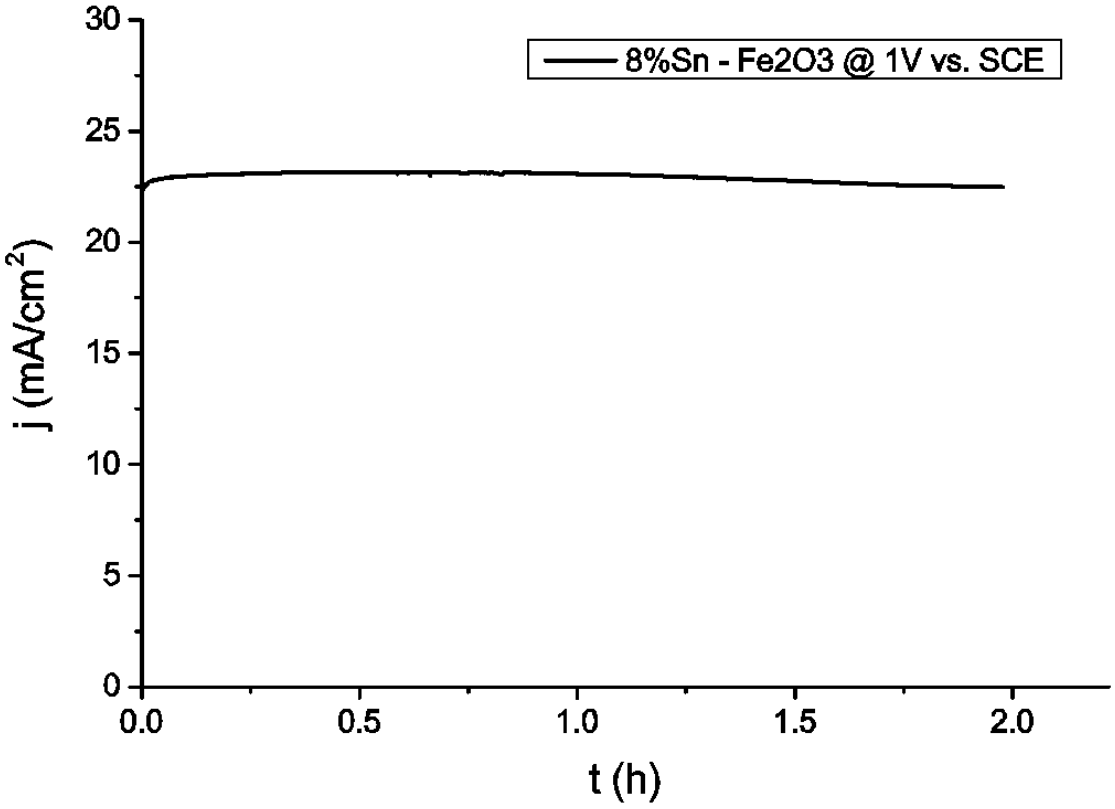

Figure 9. Chronoamperometric plot of of the 7.7 at. % Sn-doped sample at 1 V *versus* SCE during a 120 min electrolysis.

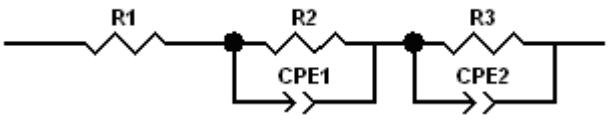

Scheme 1. Electrical model used to fit EIS data

Appendix A – Graphical Table of Content

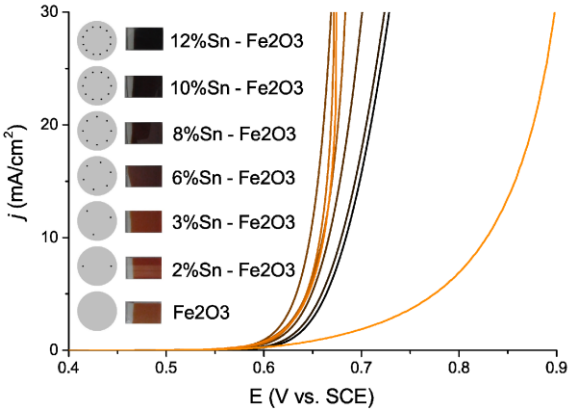

Table 1. EDS results.

Sn/(Sn+Fe) at. %	1.2±0.1	1.9±0.1	3.0±0.1	6.2±0.1	7.7±0.2	9.5±0.1	12.4±0.2

Table 2. Calculation of cell parameters* from XRD peaks.

Sn %	*a* (Å)	*c* (Å)
0.0	5.0331±0.0003	13.843±0.005
1.2	5.0391±0.0005	13.826±0.005
1.9	5.0395±0.0003	13.818±0.004
3.0	5.0450±0.0003	13.81±0.01
6.2	5.0564±0.0003	13.80±0.01
7.7	5.0613±0.0004	13.771±0.006
9.5	5.0673±0.0004	13.771±0.004
12.4	5.0769±0.0005	13.768±0.004

* *b* is not reported since *a*=*b*

Table 3. Direct and indirect optical band gaps.

Sn %	0.0	1.2	1.9	3.0	6.2	7.7	9.5	12.4
Direct E_g (eV) ± 0.02	2.19	2.19	2.19	2.19	2.18	-	-	-
Indirect E_g (eV) ± 0.01	1.64	1.66	1.65	1.64	1.57	1.48	1.29	1.19

Table 4. Onset overpotential η (j=1 mA/cm^2) and Tafel slope b.

Sn at. %	0.0	1.2	1.9	3.0	6.2	7.7	9.5	12.4
η (mV)	498±10	446±5	449±3	445±4	441±6	453±2	463±7	468±8
b (mV/dec)	102±1	56.8±0.1	48.4±0.1	55.5±0.1	47.9±0.3	49.5±0.1	49.0±0.3	50.3±0.7

Appendix B – Supporting Information

Sample – Sn at. %	D (110) nm	D (300) nm
0	106 ± 2	81 ± 2
1.2	88 ± 3	54 ± 1
1.9	79 ± 3	75 ± 2
3	95 ± 2	73 ± 1
6.2	90 ± 2	74 ± 2
7.7	91 ± 2	72 ± 2
9.5	120 ± 3	66 ± 2
12.4	101 ± 2	86 ± 2

Table S1. Grain size estimated from the (110) and the (300) XRD peaks using the following Scherrer relation: $D = 0.9\lambda / \beta x \cos(\theta)$ where D is the grain size, λ is the incident X-ray radiation and β is the FWHM of the lorentzian fitted peak. Estimation of D for (110) and (300) differs because peaks are more broadened for the (110) direction, indicating the presence of elongated crystalline domains.

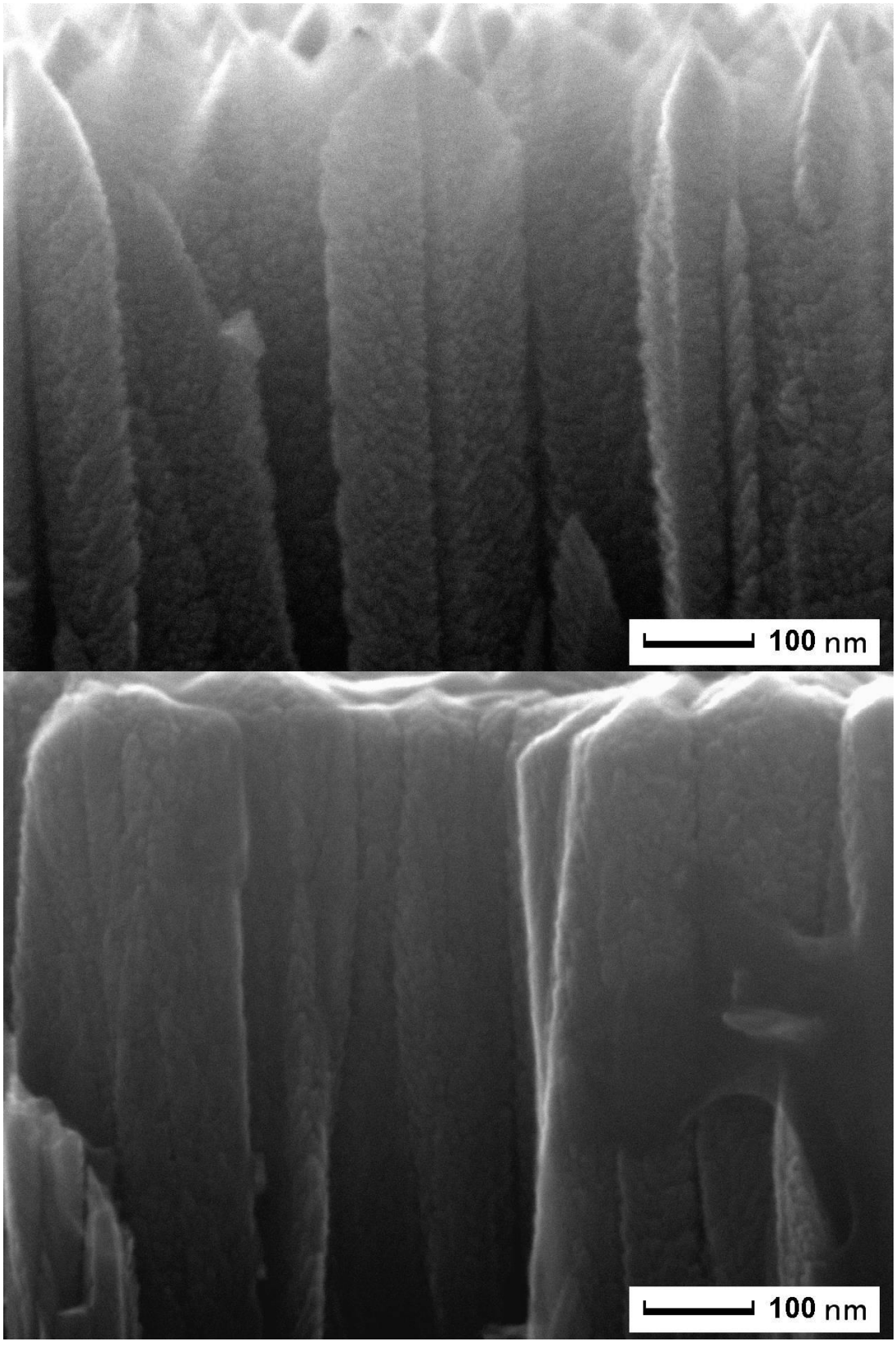

Figure S1. Details of the cross-sections for 0% (top) and 12% (bottom).

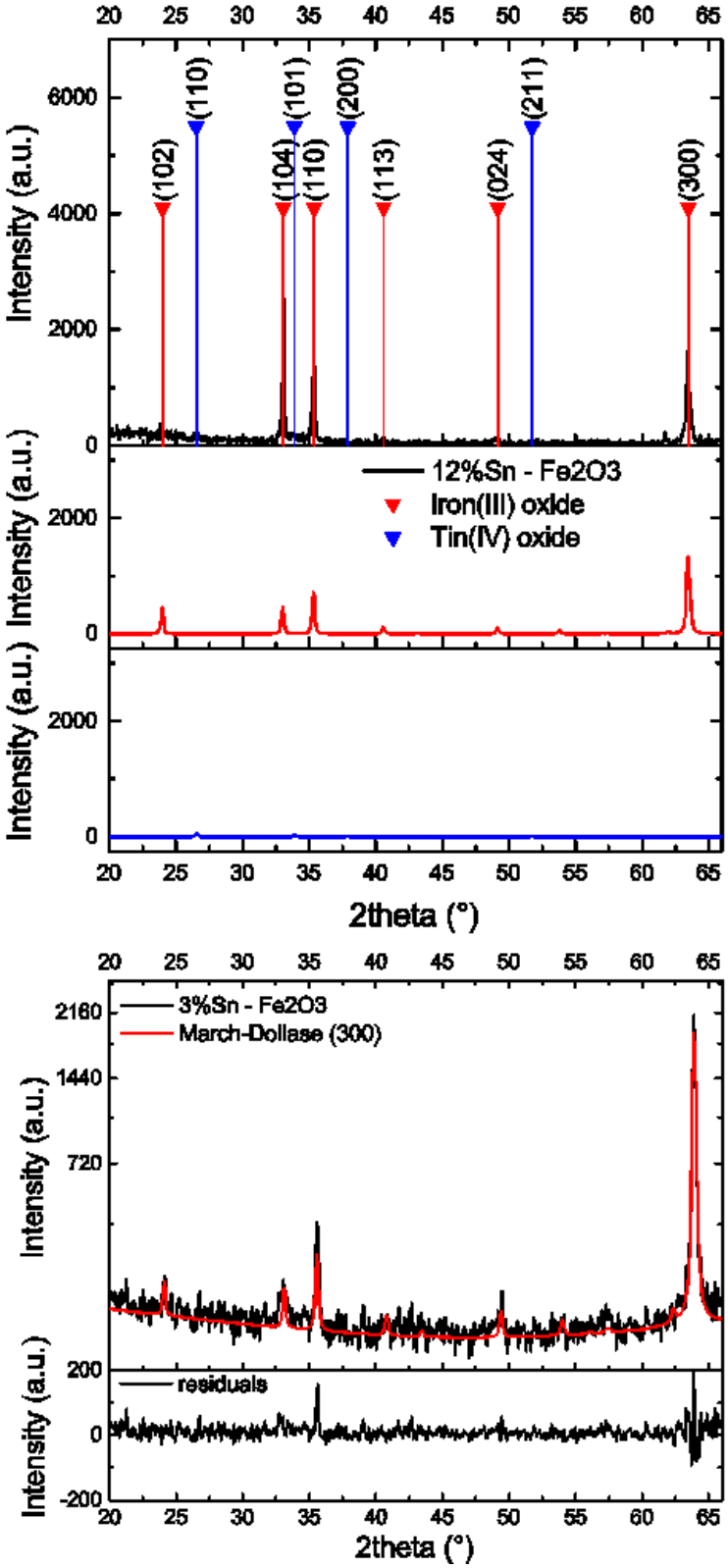

Figure S2. (top) XRD spectrum of the sample with higher tin content (12.4 at. %). The positions of the main reflections of iron(III) oxide and tin(IV) oxide crystalline structures are here indicated. The contribution of the two possible phases is shown in the bottom panels for Fe_2O_3 (red) and SnO_2 (blue). On the base of this analysis the presence of tin oxide as a distinct phase can be excluded. (bottom) XRD spectrum of the 3 at. % sample with the fitting function (red line) obtained using a

March–Dollase texture profile about the (300) hematite plane to account for preferential orientation. A square root scale was used for the vertical scale to emphasize the less intense signals. In the bottom panel the fit residuals are shown. For both the analyses the Maud software was used to perform Rietveld refinement.

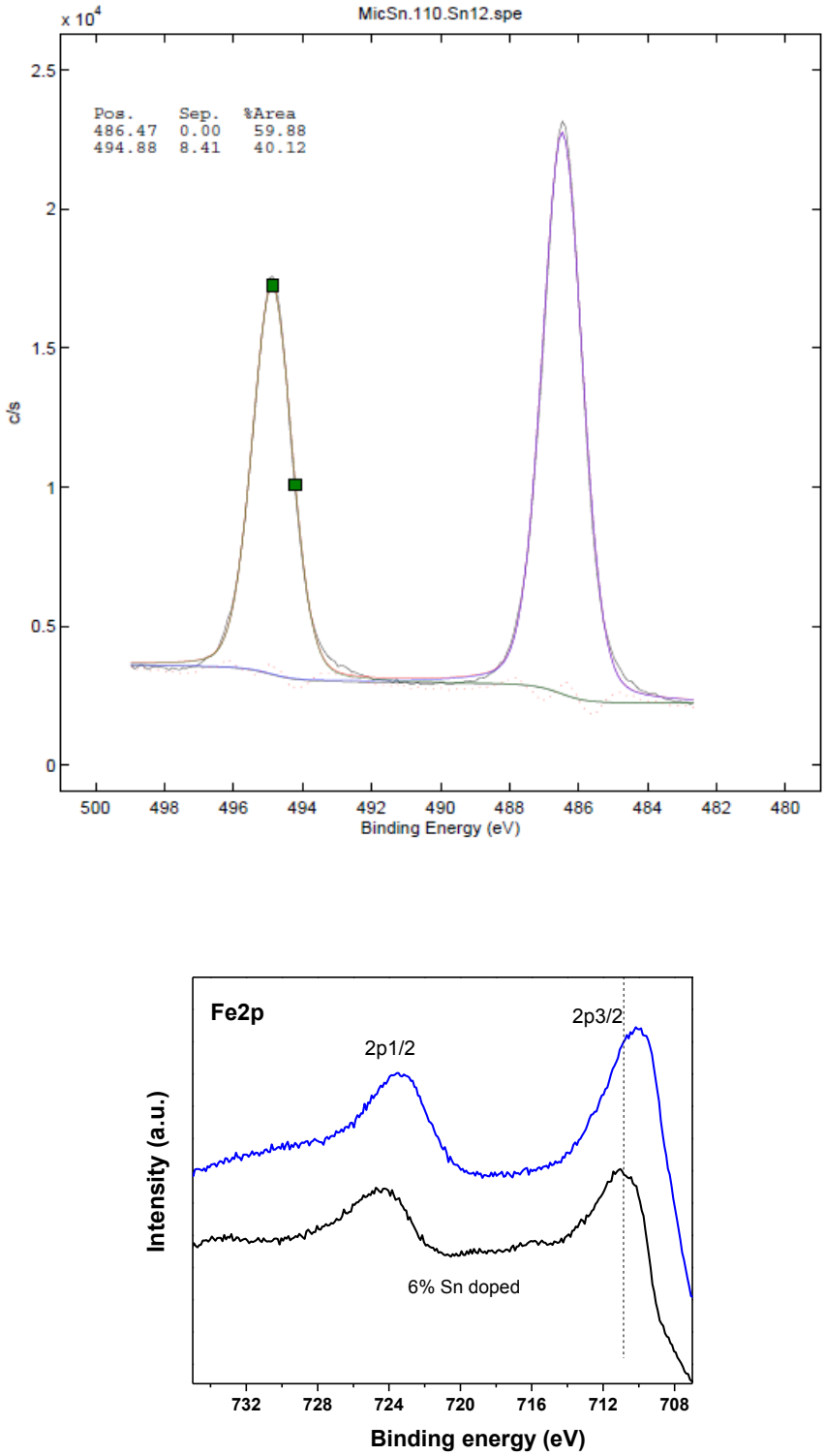

Figure S3. XPS spectra: Sn3d5/2 for 12 at. % sample (top) and comparison of Fe2p signals for undoped and 6 at. % tin-doped samples (bottom).

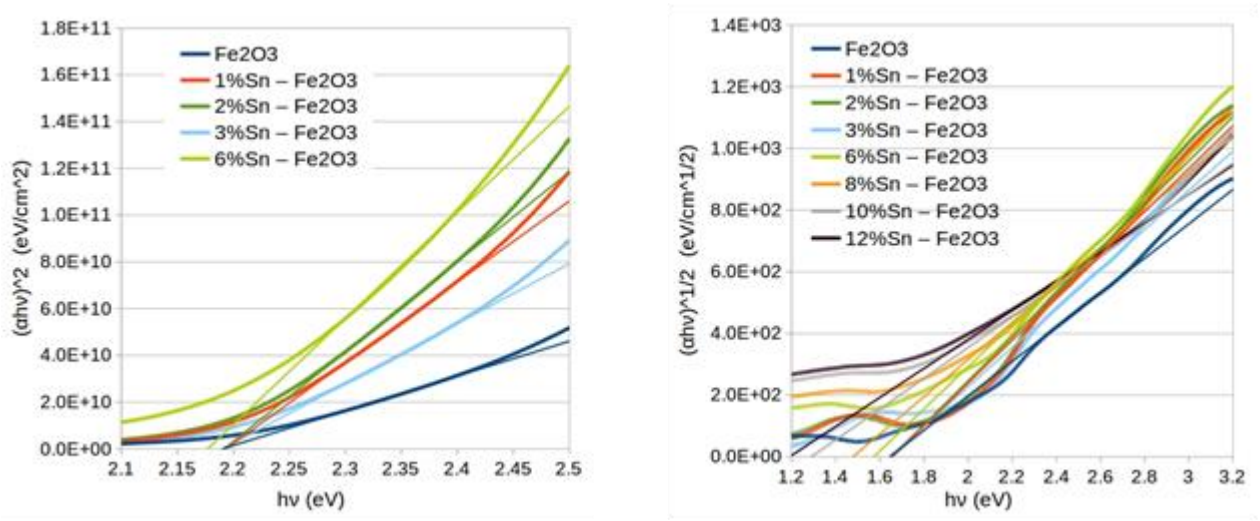

Figure S4. Tauc plots for the direct (left) and indirect (right) optical band gap.

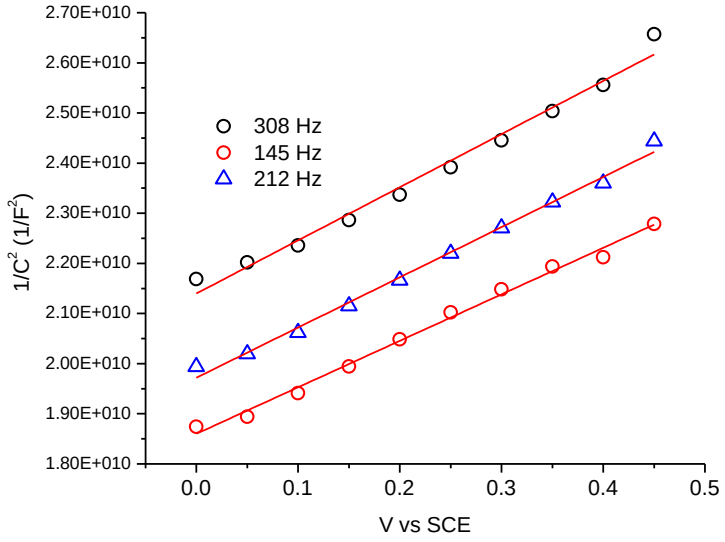

Figure S5. MS plots ($1/C^2$ vs voltage) recorded for unmodified hematite at three different frequencies. 2M KOH.

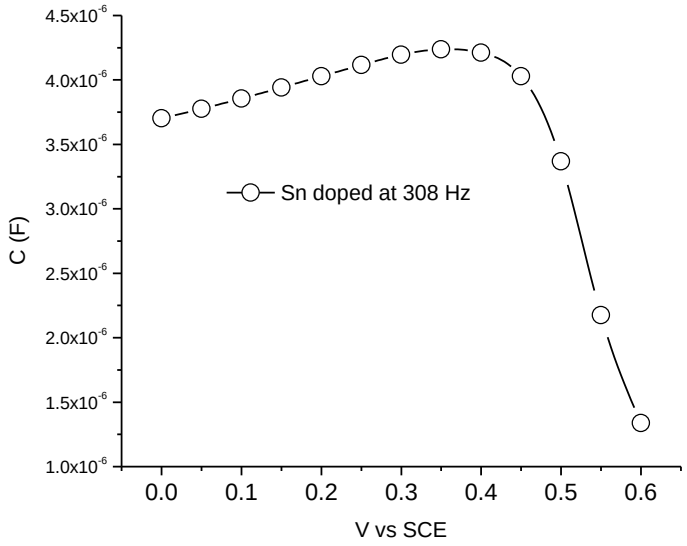

Figure S6. High frequency capacitance vs applied voltage observed at 318 Hz for the Sn modified (6.2%) hematite anode in 2 M KOH

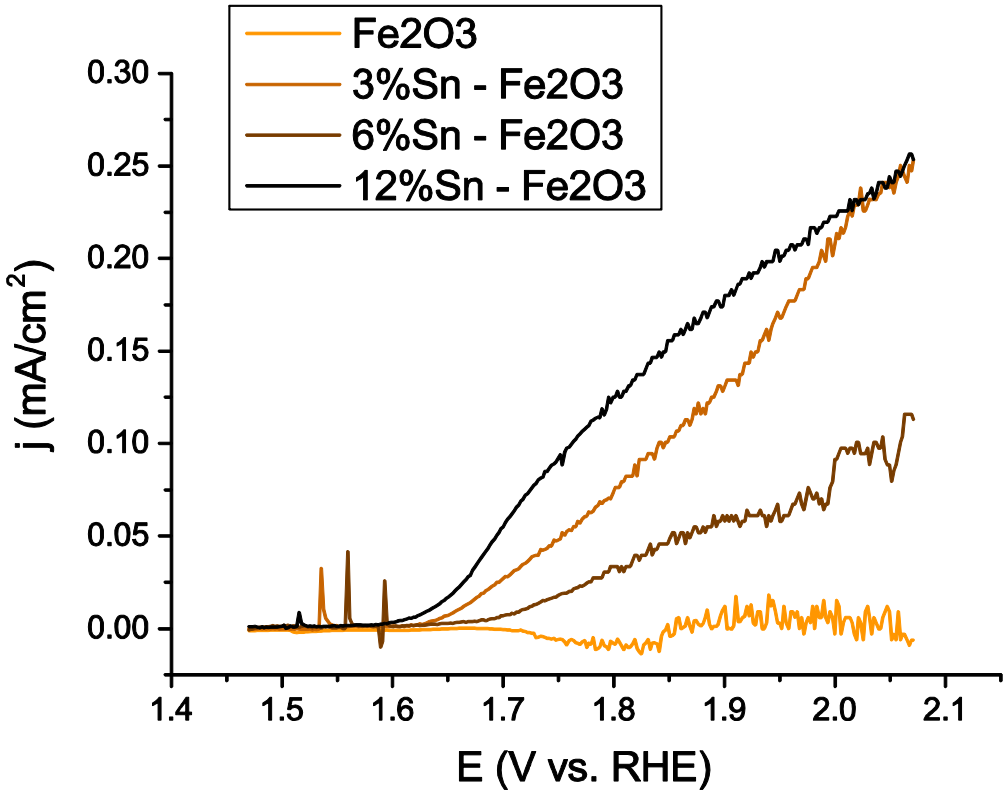

Figure S7. Photocurrent density $j_{ph} = j_{light} - j_{dark}$ measured without *iR* compensation. The illumination source was a solar simulator (AM 1.5G, 100 mW/cm^2). Although the observed photocurrents are modest, due to a combination of film thickness, compact morphology and unfavorable crystallite orientation, the trend outlines a superior charge collection efficiency in the tin doped samples.